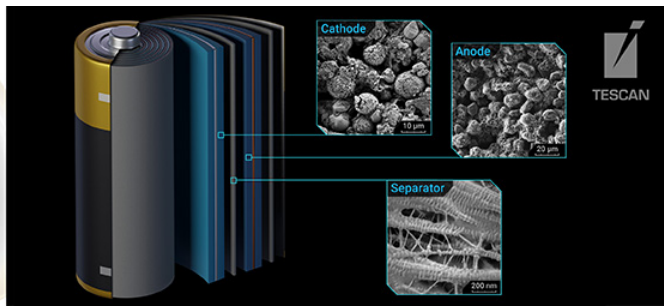
### Mapping Polar Distortions using Nanobeam Electron Diffraction and a Cepstral Approach

Megan E Holtz, Elliot Padgett, Aaron C Johnston-Peck, Igor Levin, David A Muller, Andrew A Herzing





Original Article



## Mapping Polar Distortions using Nanobeam Electron Diffraction and a Cepstral Approach

Megan E. Holtz<sup>1,2,3,\*</sup>, Elliot Padgett<sup>2,†</sup>, Aaron C. Johnston-Peck<sup>1</sup>, Igor Levin<sup>1</sup>, David A. Muller<sup>2</sup>, and Andrew A. Herzing<sup>1</sup>

#### **Abstract**

Measuring local polar ordering is key to understanding ferroelectricity in thin films, especially for systems with small domains or significant disorder. Scanning nanobeam electron diffraction (NBED) provides an effective local probe of lattice parameters, local fields, polarization directions, and charge densities, which can be analyzed using a relatively low beam dose over large fields of view. However, quantitatively extracting the magnitudes and directions of polarization vectors from NBED remains challenging. Here, we use a cepstral approach, similar to a pair distribution function, to determine local polar displacements that drive ferroelectricity from NBED patterns. Because polar distortions generate asymmetry in the diffraction pattern intensity, we can efficiently recover the underlying displacements from the imaginary part of the cepstrum transform. We investigate the limits of this technique using analytical and simulated data and give experimental examples, achieving the order of 1.1 pm precision and mapping of polar displacements with nanometer resolution.

Key words: 4D STEM, ferroelectrics, nanobeam electron diffraction

#### Introduction

Materials with polarity—that have a crystal structure with broken inversion symmetry—comprise a fundamentally interesting and technologically relevant space, including ferroelectrics, piezoelectrics, and many two-dimensional materials. In many of these systems, the polar displacements exhibit spatial variations, with examples including interfaces, such as electrode/substrate or domain walls (Stemmer et al., 1995a; Zheng et al., 2007; Catalan et al., 2011; Han et al., 2014; Holtz et al., 2017; Xu et al., 2020), antiferroelectrics, relaxor ferroelectrics, or materials with charge density waves, which feature nanoscale-correlated polar disorder (MacLaren et al., 2013; Hovden et al., 2016; Baggari et al., 2018; Eremenko et al., 2019; Kumar et al., 2021), nanostructured materials exhibiting distinct types of polar order (Naumov et al., 2004; Schilling et al., 2009; Nahas et al., 2015; Liu et al., 2017), and superlattices with dimensional confinement that can create or destroy ferroelectric vortices (Yadav et al., 2016, 2019; Holtz et al., 2021). In all these cases, understanding structure-property relationships is aided by localized measurement of the polarization at the atomic and nanometer scales.

While bulk Bragg diffraction methods permit high-precision measurements of crystal structure, the determination of local structural variations is challenging. Combining diffraction-based techniques with simulation (such as reverse Monte Carlo) is one promising approach (Eremenko et al., 2017), where the structure is represented using a large atomic configuration and the local and nanoscale orders are determined via the comparison of calculated and experimental signals.

However, such macroscopic methods cannot provide direct, localized measurements of the crystal structure.

The ability to directly characterize the local atomic order, including the local polarity, is a difficult problem (Billinge & Levin, 2007). Imaging of structural projections in a transmission electron microscope (TEM) is widely used to for this purpose (Stemmer et al., 1995a, 1995b; Jia et al., 2007, 2008). In particular, atomic-resolution annular dark field (ADF) scanning TEM (STEM) is a powerful tool for imaging atomic columns due to its straightforward and incoherent contrast mechanism which scales with the atomic number (Crewe et al., 1970; Howie, 1979; Kirkland et al., 1987; Voyles et al., 2002; Zuo & Spence, 2017). Because ADF STEM excels at providing the locations of heavy cations, ferroelectric displacements can be directly measured in many materials (Borisevich et al., 2010; Chang et al., 2011; Nelson et al., 2011). Measuring oxygen displacements is also critical for understanding ferroelectricity. Although this is generally not feasible from ADF due to weak scattering by the oxygen atoms, it can be achieved with bright field imaging (LeBeau et al., 2009), annular bright field (ABF) imaging (Findlay et al., 2009; Aso et al., 2013), or differential phase contrast (DPC) techniques using segmented detectors (Lazić et al., 2016; Campanini et al., 2020; Kumar et al., 2021). However, atomic-resolution STEM is sensitive to scan distortions as well as specimen tilt and thickness (Muller et al., 2006; Kimoto et al., 2010; Zhou et al., 2016; Bürger et al., 2020) all of which compromise the accuracy of the measurement. It also requires a large electron dose to achieve a signal-above-background that is sufficient for fitting positions

<sup>&</sup>lt;sup>1</sup>Material Measurement Laboratory, National Institute of Standards and Technology, 100 Bureau Drive, Gaithersburg, MD 20899, USA

<sup>&</sup>lt;sup>2</sup>School of Applied and Engineering Physics, Cornell University, 142 Sciences Drive, Ithaca, NY 14853, USA

<sup>&</sup>lt;sup>3</sup>Department of Metallurgical and Materials Engineering, Colorado School of Mines, 1301 19th Street, Golden, CO 80401, USA

<sup>\*</sup>Corresponding author: Megan E. Holtz, E-mail: mholtz@mines.edu

<sup>†</sup>Current address: Chemistry and Nanoscience Center, National Renewable Energy Laboratory, 15013 Denver West Parkway, Golden, CO 80401, United States

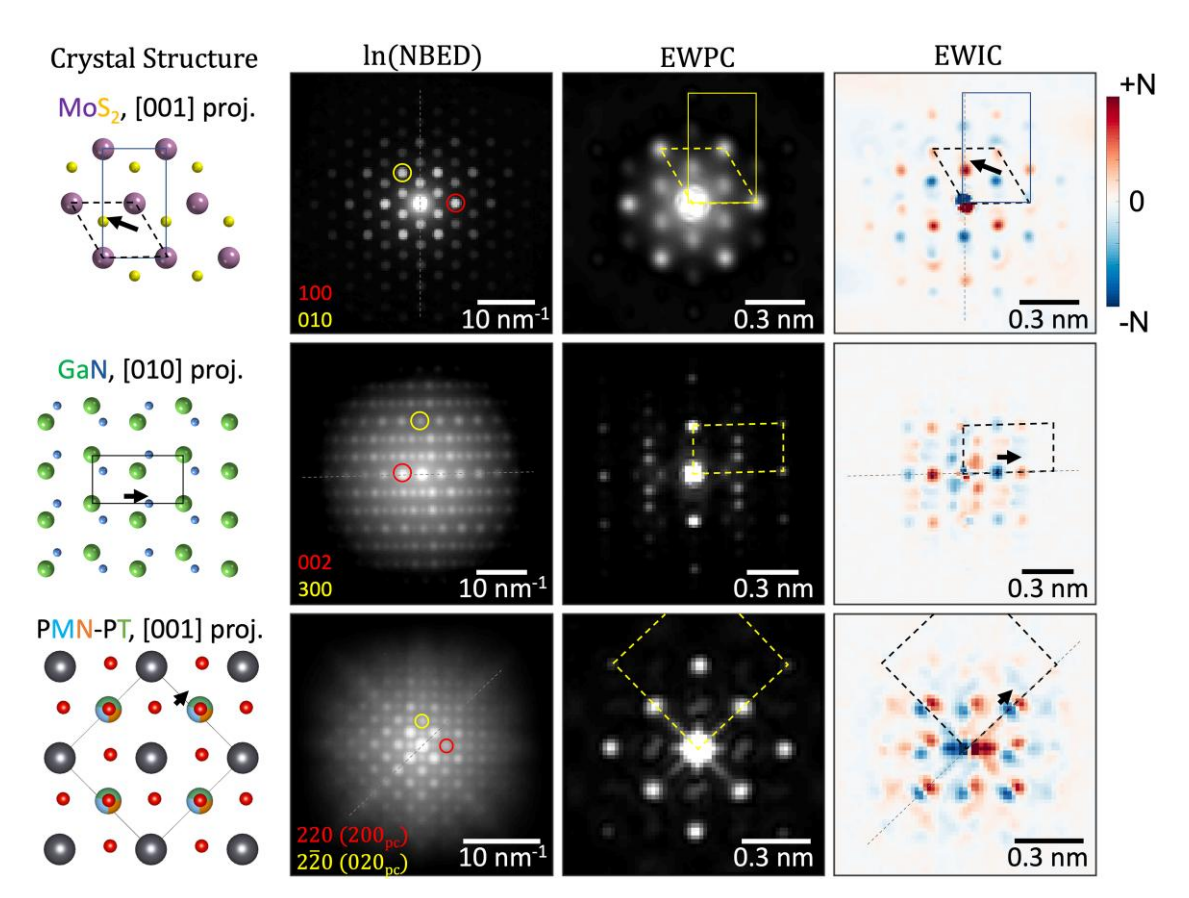


**Fig. 1.** An overview of the cepstral transforms providing interatomic distances and polarity and how they relate to the crystal structure for three different materials: MoS<sub>2</sub>, GaN, and PMN-PT. The first column shows the crystal structure to scale, with the unit cells marked starting from the center of the transforms (for MoS<sub>2</sub>, two unit cells are marked). The second column is the logarithm of the nanobeam electron diffraction pattern (ln(NBED)), with circled spots corresponding to the indices labeled in the bottom left. Because these materials are noncentrosymmetric, there is symmetry breaking in the diffraction pattern. The third column is the absolute magnitude of the Fourier transform of the ln(NBED), or exit wave power cepstrum transformation (EWPC) or "gamnitude," which is similar to a pair distribution function. The final column shows the imaginary component of the Fourier transform of the ln(NBED), or exit wave imaginary cepstrum (EWIC) highlighting polarity and symmetry breaking in the crystals. Arrows corresponding to the polar displacements are shown for both the EWIC and the crystal structure. Dashed lines on the NBED and EWIC columns are mirror planes.

of the atomic columns. Finally, atomic-resolution STEM typically covers only small fields of view to maintain the required spatial sampling, making it unsuitable for mapping of micrometer-scale polar domain structures.

Scanning nanobeam electron diffraction (NBED) bridges the gap between bulk diffraction, which achieves highprecision measurements over large regions, and atomic-scale imaging, which covers smaller fields of view at high resolution. NBED combined with new, fast, pixelated STEM detectors [so-called 4D STEM because it collects the diffraction pattern  $(k_x, k_y)$  at every scan position (x, y)] can achieve crystallographic measurements with unit-cell-sized spatial resolution over relatively large fields of view for STEM (micrometers) (Ophus, 2019). NBED also allows new avenues for measuring polarity and electric fields (Yadav et al., 2019). Because of the possible breaking of Friedel's law in electron diffraction from noncentrosymmetric materials (Miyake & Uyeda, 1955), measuring the relative intensities of [hkl] and [hkl] reflections can yield the direction and relative magnitude of the polarization vector or symmetry breaking (Wicks & Lewis, 1968; Serneels et al., 1973; Tanaka, 1975; Lebeau et al., 2011; Tsuda et al., 2013; Yadav et al., 2019; Deb et al., 2020). Figure 1 provides examples of several distinctly structured polar materials (with crystal structures as shown in the first column) generating NBED patterns that exhibit a violation of Friedel's law (second column of Fig. 1). However, quantitative measurements of the polarization magnitude using NBED are not straightforward because the disk intensities are affected by several other factors, including dynamical diffraction or specimen tilt. For example, such effects complicate disentangling the various structural changes at domain walls (MacLaren et al., 2015).

Previously, it was demonstrated that diffraction-based techniques offered by the 4D STEM configuration combined with cepstral techniques inspired by audio processing enables robust, localized measurements of interatomic spacings (Padgett et al., 2020). This technique uses the magnitude of the Fourier transform of the flattened NBED patterns (the exit wave power cepstrum, or EWPC, transform), which produces a signal similar to a pair distribution function (PDF) in projection (third column of Fig. 1). In this case, the effects of tilt and thickness are suppressed by taking the logarithm of the NBED patterns. However, the magnitude of the Fourier transform cannot reveal asymmetrical components in the diffraction pattern arising because of the breaking of Friedel's law. The result is that EWPC can measure the tetragonality of the crystal, which can act as a proxy for polarization as previously seen in electron backscattered diffraction and Kikuchi techniques (Farooq et al., 2008), but it cannot tell the polarization direction.

Here, we develop a related, cepstral-based algorithm that extracts such asymmetrical components associated with polar distortions in the crystal, yielding the directions and magnitudes of local polar displacements. The algorithm uses the imaginary part of the Fourier transform of the flattened NBED patterns, in what we call the exit wave imaginary cepstrum (EWIC), to highlight polar components of the crystal lattice. This approach is illustrated in the final column of Figure 1, with red and blue colors indicating positive and negative components, respectively. Comparing to the crystal structure, which is to scale in the first column of Figure 1, we can see how the EWPC and EWIC transforms can detect interatomic positions with symmetric and asymmetric components, respectively.

We will discuss the mathematics behind the EWIC transform and provide an intuitive method for visualizing the resulting EWIC patterns. We will show through analytical calculations that the distance between positive and negative EWIC peaks is twice the polar displacement in the diffracting volume of the specimen and discuss how this measurement is affected by diffraction-space sampling, specimen thickness, and specimen tilt. We demonstrate approximately 1 pm precision in measured atomic displacements for thin (less than half of an elastic mean free path) specimens which are oriented with a high-symmetry zone axis aligned parallel to the electron beam. We will further apply this approach to mapping polar distortions in PbTiO<sub>3</sub> ferroelectric domains.

#### **Theory of the Complex Transform**

Previous work described the use of the EWPC transform of NBED patterns for determining interatomic spacings in crystals (Padgett et al., 2020). For a diffraction pattern, I(k), the EWPC transform is defined as follows:

$$\text{EWPC}(\boldsymbol{x}) = \big| \mathcal{F}[\ln\left(I(\boldsymbol{k})\right)] \big| = \big| \mathcal{F}[\ln\left(|\mathcal{F}[\Phi(\boldsymbol{x})]|^2\right)] \big|, \tag{1}$$

where x is the real-space position vector, k is the scattering vector, and  $\Phi(x)$  is the exit wave function. This result is conceptually similar to a PDF or Patterson function (Patterson, 1934), but, as indicated in the Introduction section, the addition of the logarithm sharpens the peaks, making the transform more robust to specimen tilt and thickness effects. For NBED conditions, where the diffraction disks are separated, I(k) was approximated as equations 6, 7, and 9 of Padgett et al., 2020, based on Ishizuka, 1982; Spence, 2013:

$$I(\mathbf{k}) = \left| \mathcal{F}[\Phi(\mathbf{x})] \right|^2 \approx \left| \Phi_p(\mathbf{k}) * (E(\mathbf{k}) \cdot V_0(\mathbf{k})) \right|^2$$
$$\approx \left| E(\mathbf{k}) \right|^2 \cdot \left| \Phi_p(\mathbf{k}) * V_0(\mathbf{k}) \right|^2. \tag{2}$$

Here, \* denotes convolution and  $\cdot$  denotes multiplication;  $\Phi_p(\mathbf{k})$  is the reciprocal-space probe function;  $E(\mathbf{k})$  is the Ewald-sphere envelope function that takes into account specimen misorientation; and  $V_0(\mathbf{k})$  is the object function based on the projected potential of the tilt-free specimen V(x), such that  $V_0(\mathbf{k}) = \mathcal{F}[\exp{(i\sigma V(x))}]$ , where  $\sigma$  is the scattering cross section.

This form of I(k) highlights several useful properties of the cepstral transform. The logarithm in the transform separates multiplied signals additively, isolating the effects of specimen tilt, E(k), from the lattice component,  $V_0(k)$ . The Fourier transform of the diffracted disks converts the lattice-spacing

information into sharp, real-space points, enabling dose-efficient and precise measurements of interatomic distances.

The parameter of interest here is the polarity of the crystal  $(V(x) \neq V(-x))$ . Polarity appears in electron diffraction patterns as an antisymmetrical component, such that  $I(k) \neq I(-k)$ . If Friedel's law is violated, the diffracted intensity can be represented as  $I(k) = I_{\text{sym}}(k) + I_{\text{anti}}(k)$ , where  $I_{\text{sym}}(k)$  is the symmetric part of the diffraction pattern and  $I_{\text{anti}}(k)$  is its antisymmetric part.

While the EWPC transform excels at extracting interatomic distances, the magnitude of the Fourier transform of a real function is an even, centrosymmetric function, devoid of any information about asymmetry in the crystal or diffraction pattern. If we consider the (complex) Fourier transform of the function I(k), we can separate the symmetric and antisymmetric components:

$$\mathcal{F}(I(\mathbf{k})) = \mathcal{F}(I_{\text{sym}}(\mathbf{k})) + \mathcal{F}(I_{\text{anti}}(\mathbf{k})) . \tag{3}$$

The Fourier transform of a symmetric, real function is also real, whereas the Fourier transform of an antisymmetric, real function is imaginary. Thus, the first term in Eq. (3) is real and the second term is imaginary. This enables isolation of the antisymmetric component of the diffraction pattern, and thus the underlying polarity, by using the imaginary component of the Fourier transform:

$$\mathfrak{Im}[\mathcal{F}(I(\mathbf{k}))] = \mathcal{F}(I_{\text{anti}}(\mathbf{k})). \tag{4}$$

We could alternately have written this expression for  $\mathcal{F}(\ln I(k))$ , which is analogously the exit wave complex cepstrum (EWCC), although it would not be possible to write as clear of a physical interpretation for the transform as we will in Eq. 7 in the next section. Because the diffraction intensity is real and positive, the logarithm of the diffraction pattern is also a real function. Further, because the logarithm is a monotonic function,  $\ln(I(k))$  and I(k) have the same symmetry. In this section, for mathematical and conceptual simplicity, we will continue discussing the complex Patterson function,  $\mathcal{F}(I(k))$ , but the discussion is analogous to the more-useful EWCC transform.

#### Physical Picture of the EWIC Transform

To obtain a physical picture of this transform, we again consider the measured scattering distribution of electrons in diffraction space, I(k), given by the magnitude squared of the reciprocal-space exit wave function,  $\Phi(k)$ :

$$I(\mathbf{k}) = |\Phi(\mathbf{k})|^2. \tag{5}$$

Using the Wiener–Khinchin Theorem, we can then write the Fourier transform of I(k) as follows:

$$\mathcal{F}(I(\mathbf{k})) = \Phi(\mathbf{x}) \otimes \Phi^*(\mathbf{x}), \tag{6}$$

where  $\Phi^*(x)$  denotes the complex conjugate of the exit wave function and  $\otimes$  denotes the cross-correlation (or autocorrelation). This is the familiar result of the magnitude of the Fourier transform of the diffraction pattern being equivalent to the autocorrelation of the lattice potential in the weakphase approximation, where  $\Phi(x)$  is proportional to V(x) (Patterson, 1934). Notably, to reveal polarity in the diffraction pattern, the specimen must be approximated as a strongphase object—which is done for all the analytical calculations throughout this paper. Friedel's law holds in the weak-phase

approximation, and for centrosymmetric crystals. However, Friedel's law is typically violated in noncentrosymmetric crystals in electron diffraction. This is due to large electron scattering cross sections that create significant, antisymmetric third-order terms in the strong-phase approximation, even for monolayer-thin two-dimensional polar materials (Deb et al., 2020). As a result, most electron diffraction patterns that are measured from noncentrosymmetric crystals exhibit asymmetry.

To obtain polarity information (the asymmetric part of the lattice potential) from this transform, we are interested in  $\mathfrak{Sm}[\mathcal{F}(I(k))]$  (Eq. (4)). To visualize how this transform relates to the lattice, consider that

$$\mathfrak{Im}[\mathcal{F}(I(k))] = \frac{1}{2} \mathcal{F}(I(k) - I(-k))$$

$$= \frac{1}{2} [\Phi(x) \otimes \Phi^*(x) - \Phi(-x) \otimes \Phi^*(-x)].$$
(7)

This equation implies a simple graphical construction for  $\mathfrak{Im}[\mathcal{F}(I(k))]$ : it is the autocorrelation of the exit wave subtracted from the inversion of itself. For symmetric parts of the lattice, this function will be zero. The asymmetric components of the lattice generate a dipole—a positive component corresponding to the +x autocorrelation and a negative component corresponding to the -x autocorrelation. As illustrated in Figure 1 by the arrows in the rendering of the crystal structure and in the EWIC transform, the positive peak corresponds to the location of the asymmetric ion, whereas the negative peak appears at the corresponding point for an inverted unit cell. Additionally, the real part,  $\Re[\mathcal{F}(I(k))]$ , is the autocorrelation of the exit wave plus its inverted self.  $\Re[\mathcal{F}(I(k))]$  typically dominates the EWPC signal, making them appear almost identical. Thus, in this paper, we show only the EWPC in figures.

Electron diffraction is dominated by scattering from the nuclei, and therefore, the EWPC and EWIC transforms reflect internuclei (interatomic) distances. The polar direction observed in the EWIC transform is therefore sensitive to the atomic charge of the nuclei (Z), instead of the ionic or valence charge on the atom. As an example, MoS<sub>2</sub> and MoTe<sub>2</sub> would have an inverted EWIC signal from each other when the crystal structures are aligned in the same direction.

In Figure 2, we illustrate the concept of the proposed method using a diatomic 1-dimensional lattice with a potential V(x) shown in Figure 2a. This potential can be broken into its symmetric and antisymmetric components (Fig. 2b), yielding  $\Phi(x)$  with real and imaginary parts shown in Figure 2c. The magnitude of the Patterson function is equivalent to the magnitude of the autocorrelation of the lattice potential (Eq. (6)), which resembles the symmetric lattice potential shown in Figure 2d. The imaginary component of the complex Patterson function (IPF) returns the antisymmetric components of the lattice (Eq. (7))—as illustrated in Figure 2e.

Here, we have provided a relatively simple example for the Patterson function. The addition of the logarithm does not change the characteristic spacings of the diffraction peaks or their symmetry. As a result, the peak positions revealing interatomic spacings and polar distortions in the complex cepstra remain the same as in the complex Patterson function (although peak widths and intensities differ). To compare the IPF and the EWIC, we turn to experimental data from GaN to show a case with realistic sampling and intensities. In the

NBED pattern, I(k), we see only the brightest diffraction reflections and the central beam, but for ln(I(k)), we see spots out to high scattering angles which are attenuated by the curvature of the Ewald sphere (Fig. 2f). The magnitude of the Patterson function (PF) displays broad peaks, whereas the EWPC contains sharp, well-resolved peaks corresponding to the interatomic spacings within the unit cell for this projection direction (Fig. 2g). As discussed previously (Padgett et al., 2020), the EWPC peaks are sharper and better resolved because the logarithm enhances the relative contrast of higherorder diffraction disks, effectively extending the information limit. Comparing IPF and EWIC (Fig. 2h), the peak locations remain the same between the two methods but are far better resolved in EWIC. This effect is highlighted in the line profiles in Figure 2i through the selection box shown in black in Figure 2h. For a further comparison of the behavior of IPF versus EWIC, see Supplementary Figure 1.

#### **Materials and Methods**

The 4D STEM NBED measurements were carried out at the National Institute of Standards and Technology (NIST) and Cornell University with both microscopes operating in microprobe mode. In this mode, the illumination lenses are configured to produce a small, nearly parallel probe which prevents overlap of the resulting diffraction disks. STEM experiments at NIST were performed using a Thermo Fisher Scientific Titan 80–300 (S)TEM instrument operating with a primary beam energy of 300 keV. Scanning NBED measurements were collected with a Merlin Medipix 3RX from Quantum Detectors with a (1 to 2) ms dwell time at  $(256 \times$ 256) pixels per diffraction pattern and a bit depth of 12. STEM experiments performed at the Cornell Center for Materials Research used a Thermo Fisher Scientific Titan 60-300 (S)TEM operating with a primary beam energy of 300 keV, or 80 keV in the case of the MoS<sub>2</sub> analysis. In this setup, scanning NBED data were captured using an EMPAD detector (Tate et al., 2016) with a 1 ms dwell time at (124 × 124) pixels per diffraction pattern and a bit depth of 30. Data from both laboratories were binned by two in the spatial directions to improve the signal-to-noise ratio of the diffraction patterns.

The samples used in this study included MoS<sub>2</sub> (Figs. 1, 3), GaN (Figs. 1, 2, and 4), PbMg<sub>1/3</sub>Nb<sub>2/3</sub>O3-PbTiO<sub>3</sub> (PMN-PT) (Fig. 1), and PbTiO<sub>3</sub> (Fig. 6). Cross sectional specimens of GaN and PMN-PT were prepared by focused ion beam (FIB) lift-out using a Thermo Fisher Scientific Nova NanoLab 600. Before lift-out, protective layers of sputtered carbon followed by ion beam–deposited Pt-C were applied to the surface of the thin film. Rough milling steps were performed with 30 keV Ga<sup>+</sup> ions, and the final thinning of the sample was done at 5 keV to reduce surface damage. For these samples, data were acquired at NIST using the conditions described above.

The sample preparation and data collection details for MoS<sub>2</sub> are summarized in reference Deb et al., 2020. Similar information for the PbTiO<sub>3</sub> sample is described in references Langenberg et al., 2019; Padgett et al., 2020. For these

Certain commercial equipment, instruments, software, or materials are identified in this paper to foster understanding. Such identification does not imply recommendation or endorsement by the National Institute of Standards and Technology nor does it imply that the materials or equipment identified are necessarily the best available for the purpose.

samples, data were acquired at Cornell University using conditions described above or as described in the cited papers.

All computations were performed in MATLAB using the Curve Fitting, Image Processing, Optimization, and Signal Processing toolboxes. Essential functions and example codes are available on GitHub (Holtz, 2022). The workflow of data processing was as follows:

- 1. To maintain consistency and avoid numerical problems during the logarithm step, we first perform preprocessing of the diffraction patterns. The intensity is scaled to fit an appropriate range (zero to thousands of counts) which corrects for negative pixels on the detector and other scaling artifacts if preprocessing has altered the overall intensity. A constant value, typically 1, is then added to the raw diffraction patterns to ensure all values are greater than
- 2. The diffraction patterns are then centered numerically to avoid asymmetries caused by misalignment of the patterns on the detector. The patterns can be centered by finding the center of mass of the central disk or by minimizing the EWIC transform on lattice sites where no polar signal is expected. In this paper, the minimization approach is used, which proved to be more reliable for nonideal diffraction patterns (e.g., when the detector was saturated or where the specimen was thicker than optimal). The diffraction patterns were then centered by applying a phase shift in Fourier space. Throughout the processing, whenever the fast Fourier transform is applied, a centered Hann window is used to minimize edge effects.
- 3. Implemented in MATLAB, the EWCC transform is as follows: fftshift(fft2(fftshift(win.\*log(DP)))), where win is the centered Hann window and DP is the preprocessed two-dimensional diffraction pattern. The EWIC is the imaginary part of the EWCC, and the EWPC is the absolute value of the EWCC. Note that fftshift is used to maintain phase consistency throughout the calculation. With the use of fftshift, the convention for the center location in MATLAB is floor(*N*/2) + 1 where *N* is the size of the diffraction pattern (i.e., a [256, 256]-sized detector has a center of [129, 129]).
- 4. Peaks are then identified using an optimization method demonstrated for EWPC (Padgett et al., 2020) which is based on a minimization function. Here, the fitting must be performed for the maxima of the absolute EWPC signals as well as for the minimum and maximum values of the imaginary EWIC signal.
  - (a) In addition to the high-precision, subpixel measurement of the peak implemented in the previous EWPC package, in Figure 3, we also evaluate a "difference of 2D Gaussian" fitting algorithm, which is more accurate at small polar spacings (less than 2 pixels) but is significantly slower. The fit parameters were four spatial positions corresponding to the (x, y) coordinates of each Gaussian: two sigma parameters corresponding to the symmetrical Gaussian shapes and two intensity parameters for the height of each Gaussian—one positive and one negative.
- 5. In EWIC, we need to determine that the peaks found by the peak fitting algorithm are due to lattice polarity and not due to small random fluctuations within the fitting window (for example, noise found around a lattice spot

that should exhibit no polarity). We have tried two methods for this:

- (a) Because any component that is a real dipole in the material should also exhibit EWPC peaks at the same location, we can fit the signal represented by the EWIC×EWPC. This will suppress random noise in the EWIC signal that is not related to interatomic distances. However, if the EWPC signal is also low in this region, i.e. there is no real spot in the fitting window in this part of the sample, this will still produce spurious results.
- (b) Specify a parameter, imWt, that is a ratio of the magnitude of the EWIC spots to the EWPC spots. If there is real polarity in the sample at a scan point, imWt will be large, but if there is not, imWt will be small. We then threshold the results and only keep polarity measurements when imWt is above a threshold, which can usually be easily picked with an algorithm or by inspecting a histogram of imWt for polar and nonpolar regions and/or spots. This allows suppression of spurious results in regions with no polarity. However, picking the threshold value must be done sample to sample and may lead to subjective results.

For most microscopes, geometrical distortions of the projection lenses result in calibrations being slightly (<1%) different for the different orthogonal directions on the detector. These distortions were measured using a specimen with cubic crystal symmetry and corrected for in the subsequent analyses.

Analytical calculations of diffraction patterns were performed using atomic potentials adopted from Kirkland, 2020 and methods similar to those described in Deb et al., 2020. The calculation was executed in the strong phase approximation to maintain polarity information. Effects from tilt were incorporated using the theory presented here and in ref Padgett et al., 2020 and according to Howie, 1971; Spence, 2013; Zuo & Spence, 2017. The EWIC transform is sensitive to numerical issues, discontinuities, and resulting asymmetries that are accentuated by the logarithm and selection of the imaginary part of the signal. Therefore, care is required for the analytical calculations.

Diffraction patterns were also simulated using the Bloch wave method as implemented in MBFIT (Tsuda & Tanaka, 1999). An accelerating voltage of 300 kV and a convergence semiangle of 1 mrad were used. The total number of beams included varied with sample tilt but was at a minimum 472. The crystal structure parameters for GaN refined by Schulz and Theimann (Schulz & Thiemann, 1977) were used. Diffraction patterns were calculated at sample thicknesses in 1 nm intervals from 1 nm to 10 nm and 2 nm intervals from 10 nm to 40 nm.

#### Results

#### Polar Displacement Quantification with the EWIC Transform

We examine the behavior of the EWIC transform for polar displacements of various magnitudes by carrying out analytical calculations using the potential that describes a one-dimensional chain of atoms. The atomic chain consists of alternating species A and B (...A-B-A-B...), with the species B (which has an atomic number smaller than that of A)

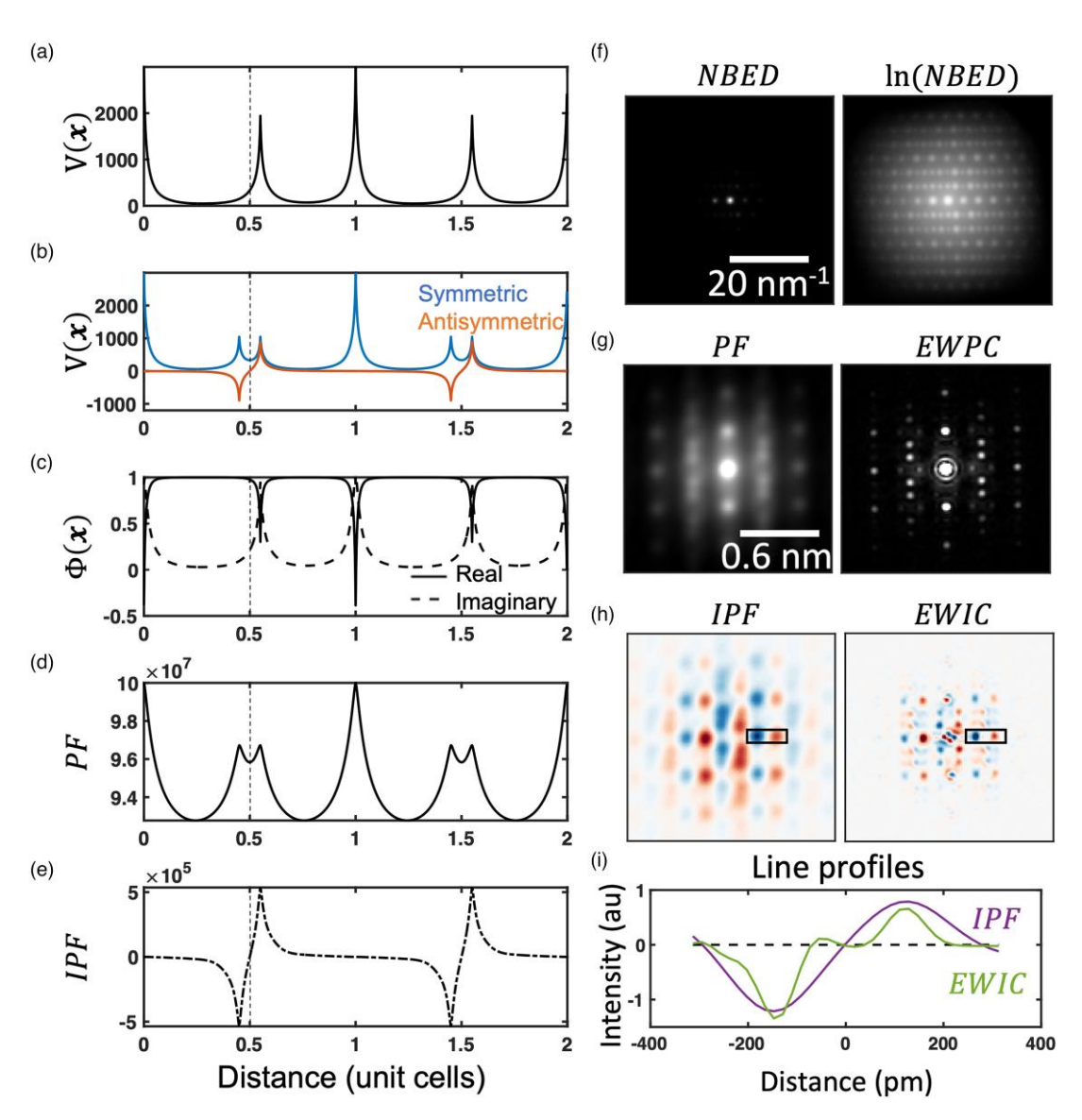


Fig. 2. Visualizing the lattice potential and the various transforms, for analytical (a–e) and experimental (f–i) data. (a) Line profiles of the potential and (b) the potential broken into its symmetric and antisymmetric components. The B site atomic position is displaced from the center of the unit cell, which is marked by the dashed line. (c) A line profile of the exit wave showing real and imaginary components. (d) The Patterson function (PF), which is the magnitude of the autocorrelation of the exit wave, which has the same symmetry as the symmetrized lattice potential shown in (b). (e) The imaginary component of the Patterson function, IPF, which effectively recovers the polar displacements shown by the antisymmetric potential in (b). Experimental data showing the transforms for GaN (f–i). (f) The NBED pattern and its logarithm. (g) The PF and exit wave power cepstrum (EWPC) transforms. (h) The IPF and exit wave imaginary cepstrum (EWIC) transforms. In both cases, the logarithm sharpens and better resolves the peaks in the transforms. (i) Line profile of the IPF and EWIC over the box shown in black in Figure 2h, displaying equivalent peak positions.

increasingly offset from a centered position (Fig. 3). For the symmetric case, where the displacement d from the center is zero, the EWPC transform (Fig. 3a) shows sharp peaks corresponding to the interatomic distances and the EWIC shows no imaginary component (Fig. 3b). Zero EWIC is expected in this case since the structure is centrosymmetric. As the displacement d increases to 0.03 unit cells and then to 0.06 unit cells, peak broadening and splitting in the EWPC transform occur, reflecting the presence of longer and shorter interatomic distances within the unit cell. In the EWIC transform, there is a dipole corresponding to this polar displacement, with the right positive and left negatives lobes flanking the centered positions. These lobes are separated by a distance equal to 2d. The polar displacement direction points from the negative to the positive peak.

For small displacements (such as d = 0.03 unit cells), the EWPC does not resolve peak splitting because of the finite width of the EWPC peak—the origins of the cepstral peak widths will be discussed in the next paragraph. The EWIC still shows a dipole with a spacing corresponding to the displacement, but, due to the finite peak width, the intensity is lower because of the peak overlap. The finite widths of the EWIC peaks impact the accuracy of peak-to-peak measurements for predicting atomic displacement: for dipole peaks located less than 2 pixels apart, the measured peak-to-peak distance in the EWIC transform using a minimization algorithm described in the methods overestimates the atomic displacement (Fig. 3c, red line). An alternative approach is to fit a "difference of Gaussian" function to model the dipole (Fig. 3c, turquoise line). This approach offers a modest improvement in the lower limit at which the

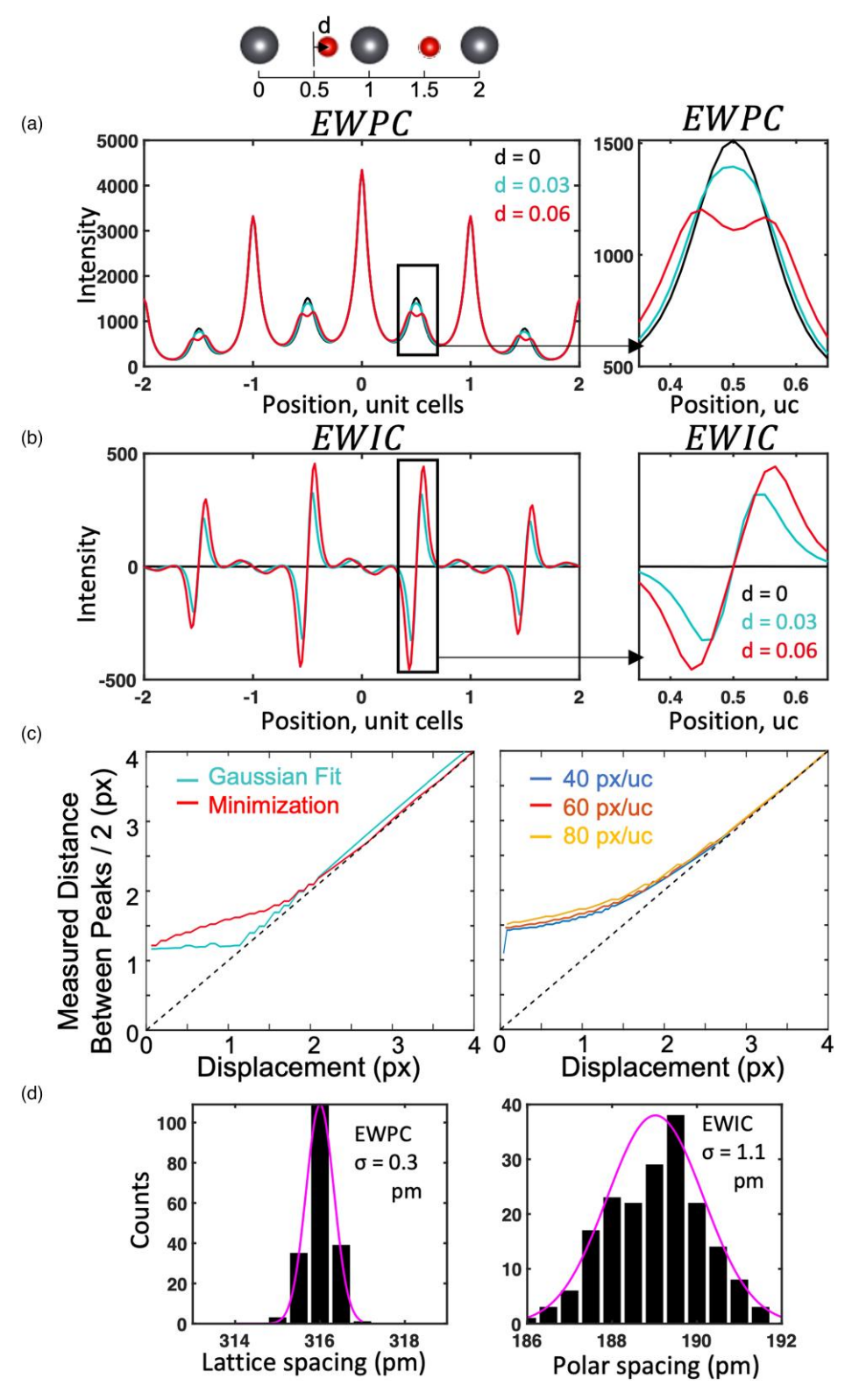


Fig. 3. The EWPC (a) and EWIC (b) transforms for a one-dimensional atomic chain with a polar displacement d = 0, 0.03, or 0.06 away from the center (as a fraction of the lattice parameter, with 60 pixels/unit cell (px/uc) sampling). On the right, there is a magnified region from the center of the unit cell showing how these transforms change with polar displacement. The EWPC transform reveals peak splitting for the larger displacement, d = 0.06, but not for the smaller displacement due to the finite peak width, which is controlled by the breadth of information measured in diffraction space. The EWIC directly measures the peak splitting, with the magnitude of splitting equal to twice the displacement distance. (c) The measured distance between the peaks divided by two compared to the displacement simulated in pixels for both Gaussian fitting and minimization algorithms (left). As the displacement becomes less than two pixels, the minimization algorithm overestimates the polar displacement, while Gaussian fitting is accurate down to the peak splitting of a single pixel although introducing fitting complexity. The accuracy is entirely controlled by sampling in the analytical calculation (c, right), since the peak width is only determined by this "effective camera length," although in experimental data, the extent of the zeroth-order Laue zone that is measured can also be a limiting factor. Thus, sampling the data to ensure expected peak distances which are larger than ideally two pixels minimizes these artifacts. (d) The histograms of lattice spacing measured by EWPC and the precision of the polar spacing measured by EWIC for an experimental dataset of monolayer MoS<sub>2</sub> shown with a Gaussian fit. The standard deviation,  $\sigma$ , is indicated for each.

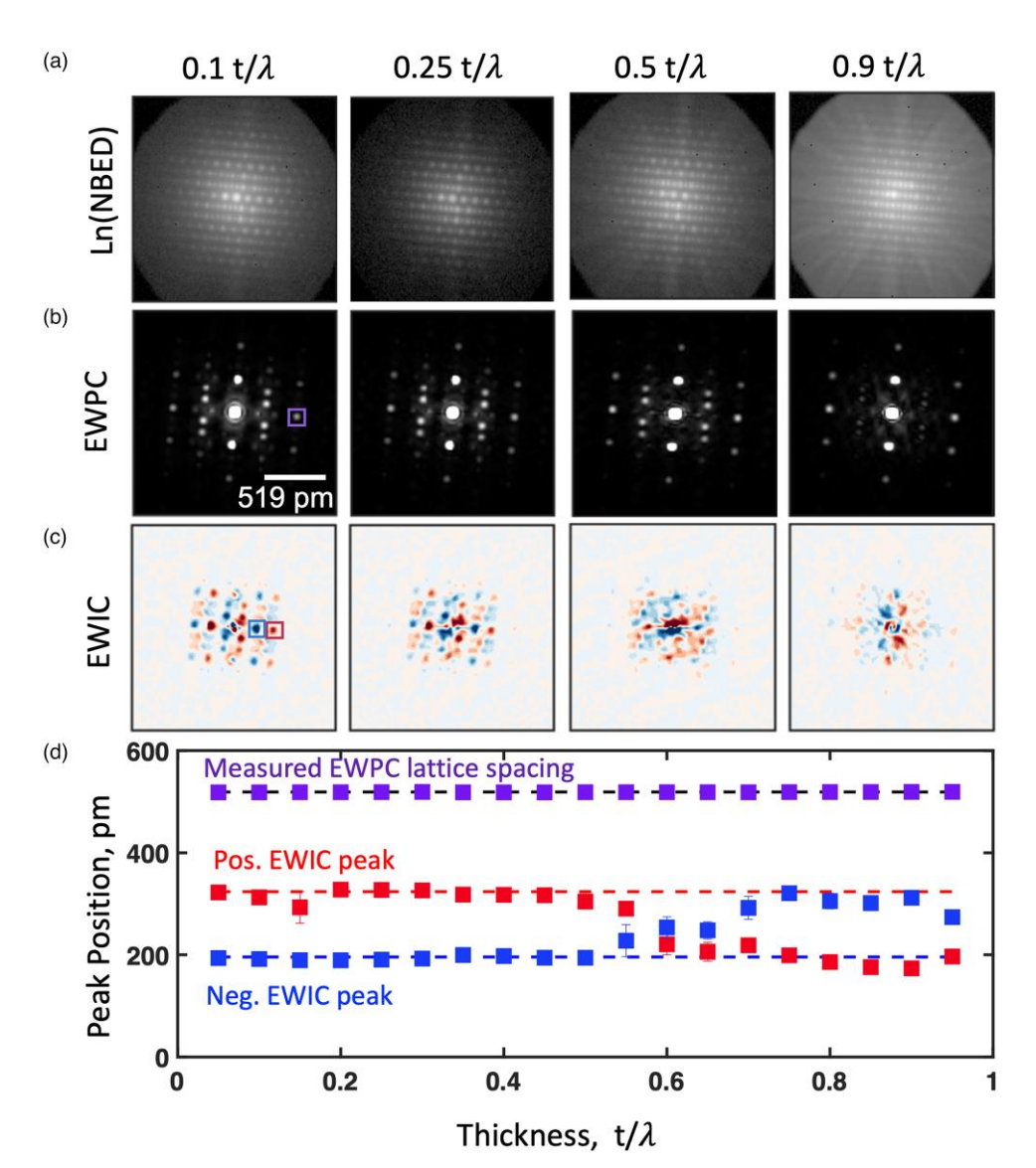
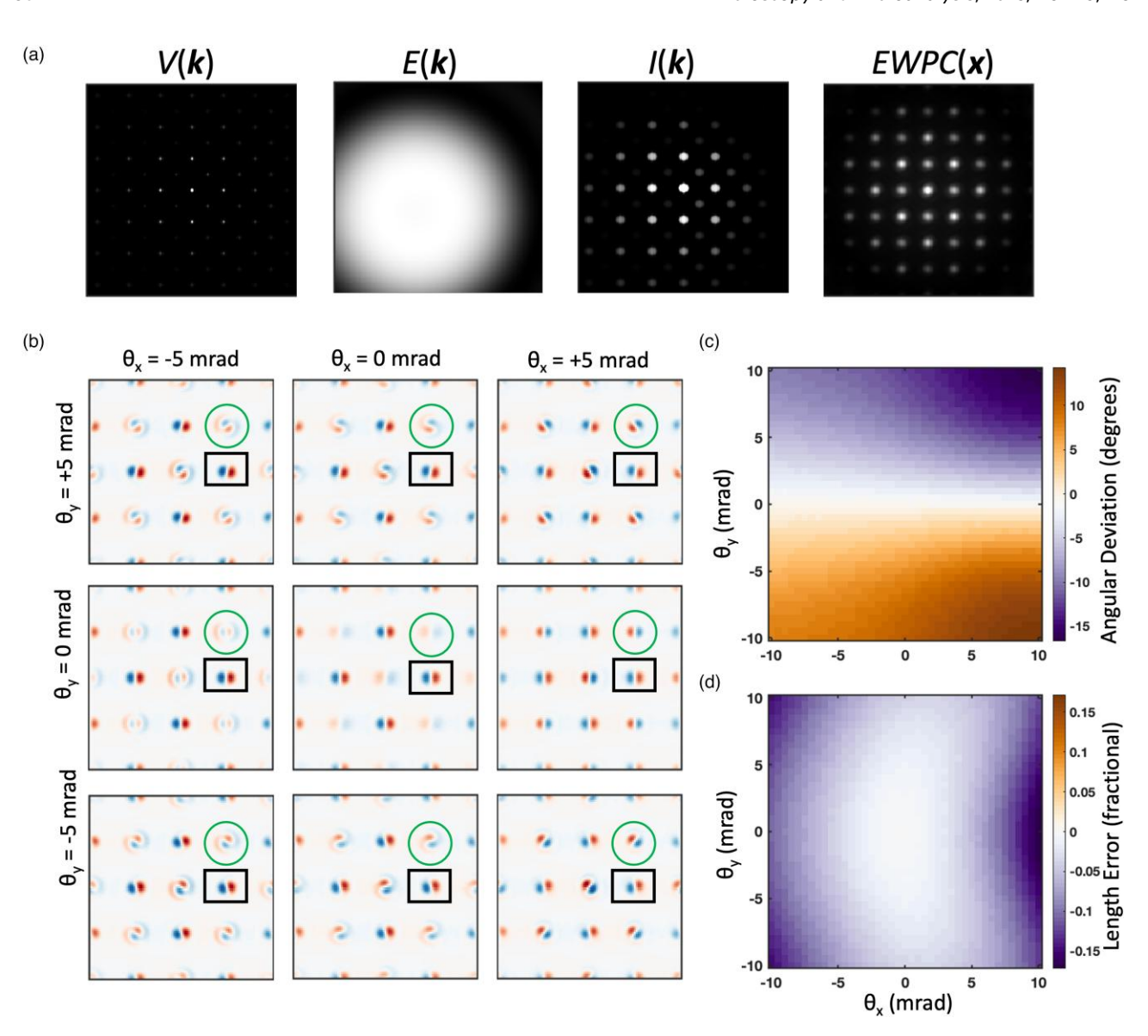


Fig. 4. The (a) NBED, (b) EWPC, (c) EWIC, and (d) measured lattice spacings and polar displacements as a function of specimen thickness measured experimentally for the GaN sample, with thickness determined by EELS. The EWPC peak is measurable throughout the range of thicknesses, reliably extracting the lattice parameter, as expected from previous results. The EWIC transform has clear spots for the two thinnest-sample datasets but becomes increasingly unclear for  $t/\lambda \ge 0.5$ . We can accurately determine peak spacing of up to  $t/\lambda = 0.5$ , but the measurements become unreliable above that thickness. Because the EWIC transform is sensitive to relative changes of intensities for the diffraction pattern spots, it is also sensitive to the effects of multiple scattering. Error bars are standard error in the mean of the measurements from that thickness.

displacement can be measured accurately, down to about d = 1.25 pixels; however, there is significant added complexity, fitting parameters, and computational time introduced by the "difference of Gaussian" fits. Here, we use the minimization function.

The cepstral peak width—and thus the smallest resolvable distance—is related to the highest frequencies in diffraction space which are included in the transform. Because polar displacements in crystals can be as small as 10 pm, adequate sampling in diffraction space is essential to achieve well-separated and sharp spots. There are two main sampling effects to consider: the breadth of the cepstral spot and the pixel size in cepstral space. The cepstral spot breadth is ultimately limited by the extent of the zeroth-order Laue zone captured by NBED. The highest order of measurable diffracted disks is limited by beam voltage and specimen thickness, with higher voltages

and thinner crystals yielding sharper cepstral spots. In practice, the highest order of diffracted disks measured may also be limited by the upper angular bound of the detector or by the windowing function used in the Fourier transform. In this case, the pixel size is limiting. The cepstral pixel size is approximately equal to the wavelength of the incident electron beam divided by the total angular range of the detector; that is, the sampling in this space can be controlled by adjusting the camera length. For a 300 keV beam with a wavelength of 1.97 pm and a ferroelectric displacement of 10 pm, the half angular range of the detector should be nearly 100 mrad, which is a relatively large angle. Because the diffracted disks rarely extend beyond the first 50 mrad, increasing the cepstral sampling can also be accomplished by using a detector with more pixels, padding after windowing, or by using subpixel measurement techniques (as done here). The sharpness of the peaks should be optimized using



**Fig. 5.** Analytical calculations showing the effect of specimen mistilt on EWIC transform for a two-dimensional version of the potential in Figure 3. (a) The reciprocal space potential  $V(\mathbf{k})$  is modulated by the tilted (off-center) Ewald sphere function  $E(\mathbf{k})$  and convolved with the probe function which gives the diffraction pattern  $V(\mathbf{k})$  (Eq. (2)). The EWPC transform is shown on the right. (b) The EWIC transform for tilts around the axes perpendicular  $(\theta_x)$  and parallel  $(\theta_y)$  to the polarization direction. As the specimen is tilted, lattice peaks show additional dipoles corresponding to the asymmetry introduced in the data by the tilt. These dipoles point in the direction of the tilt. The sites which have polar dipoles from the lattice (shown in the box) don't display a full change in direction like the lattice peaks but exhibit significant angular deviation, which is quantified in (c). The fractional error in the length of the dipole is shown in (d), which is consistent with the trend towards shortening the magnitude of the polar displacement.

high primary beam energies, thin specimens, and short camera lengths that collect slightly more than the entire zeroth-order Laue zone. Detectors with larger numbers of pixels may be advantageous for this method. In Figure 3, because we are using an analytical calculation with arbitrarily high sampling, we are ultimately limited by cepstral pixel size as shown in the right panel of Figure 3c.

Under ideal experimental conditions for a thin, on-axis crystallite with well-separated asymmetrical lattice components (making ideal sampling straightforward), we can find the precision of EWPC lattice–parameter and EWIC polarity measurements. Figure 3d presents simultaneous EWPC and EWIC measurements for monolayer MoS<sub>2</sub>, yielding standard deviations of 0.3 pm and 1.1 pm for the EWPC and for the EWIC peak positions, respectively.

#### Tilt, Thickness, and Miscentering Effects on EWIC

Next, we turn to the behavior of the transform under a range of realistic experimental conditions. We investigated the effect of specimen thickness by collecting experimental data for a GaN wedge–shaped specimen with a ratio of thickness t to the inelastic mean free path  $\lambda$  varying from 0.1 to 1 (Fig. 4). This ratio was determined using electron energy loss spectroscopy (EELS). The inelastic mean free path for a 300 keV electron beam in GaN is 90 nm if estimated using the Malis method (Malis et al., 1988) and 120 nm per the free-electron estimate (eq. 3.58 of Egerton, 2011). We should note that we used EELS to measure the thickness in terms of inelastic mean free path for experimental convenience but the more relevant parameter for diffraction patterns is the elastic mean free path. Because the ratio of elastic to inelastic mean

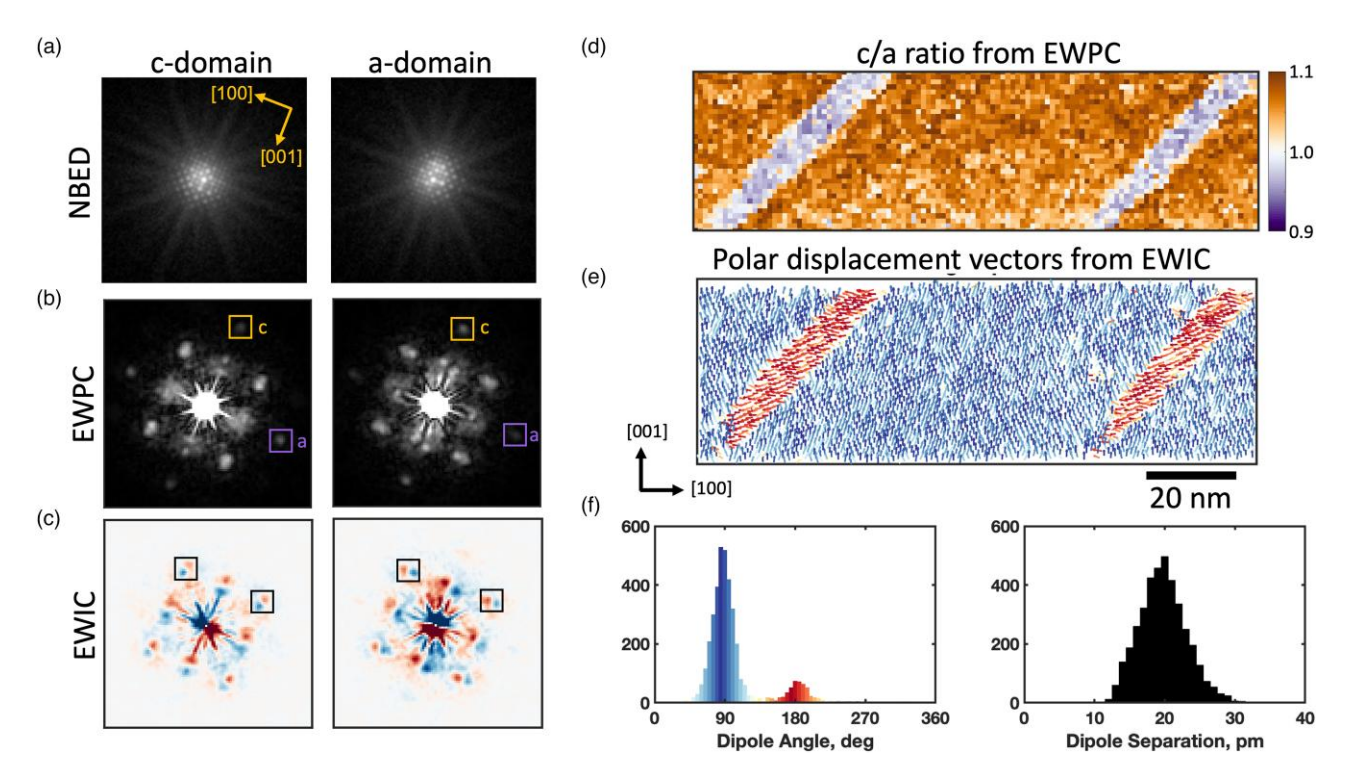


**Fig. 6.** An example of lattice and polarity mapping from scanning NBED measurements of PbTiO<sub>3</sub>. Example (a) NBED, (b) EWPC, and (c) EWIC from a domains (in-plane polarization) and c domains (out of plane polarization) in PbTiO<sub>3</sub>. In the EWPC transform, in-plane and out-of-plane (a and c) lattice spots are marked. In the EWIC transform, the spots representing a polar dipole associated with Pb-Ti off-centering are indicated. (d) The c/a lattice-parameter ratio from EWPC, highlighting the c (orange) and a domains (purple). (e) The polar displacement vectors measured from EWIC, with colors corresponding to the dipole angles shown in the histogram below. (f) Histograms of the polar dipole directions and separations. The dipole separation is (19 ± 4) picometers, overestimating the expected displacement (15 pm), likely due to undersampling. The reported error is the standard deviation.

free paths varies as 20/Z, where Z is the atomic number (see Eq. 5.66 in Reimer & Kohl, 2008), and the effective Z of GaN is 19, conveniently, in this specimen, the inelastic and elastic mean free paths are about the same and the indicated thicknesses also correspond to the elastic mean free path.

The NBED patterns for several  $t/\lambda$  values are presented in Figure 4a. The EWPC transform, shown in Figure 4b, reveals that while some peak intensities decrease markedly for larger thicknesses, the peak locations are unchanged. For example, the position of the EWPC peak marked with a purple box remains constant across the entire range of measured thicknesses (purple points in Fig. 4d). Error bars indicating the standard error in the mean are smaller than the symbol size.

The EWIC transform as a function of thickness (Fig. 4c) displays similar peaks for  $t/\lambda$  equal to 0.1 and 0.25, whereas the peaks become less clear for larger thicknesses. Unlike the EWPC transform, EWIC relies on relative intensities of diffracted disks to determine the polarity, and, therefore, multiple scattering and dynamical diffraction obscure the asymmetry. Figure 4d presents the positions of the positive and negative EWIC peaks (marked in red and blue, respectively, as a function of thickness); the dashed line shows the nominal positions of these peaks. The peak measurement is robust up to  $0.5t/\lambda$  but becomes unreliable for larger thicknesses, displaying contrast inversion. The origin of contrast inversion likely stems from thickness fringes in the Friedel pairs in the diffraction pattern (Howie & Whelan, 1961; Howie, 1971; Serneels et al., 1973). We expect that this contrast reversal will be a general effect due to dynamical scattering inherent to Friedel's law breaking and will likely

limit all polarization mapping techniques based off of relative spot intensities.

While there may be dependence on the specific material, these tests suggest that valid EWIC measurements require samples thinner than roughly 0.5 elastic mean free paths to avoid multiple scattering artifacts including contrast inversion. We did not find any limitation in the very small thickness limit, where we might expect the diffraction intensity to behave in a more kinematical manner and Friedel symmetry breaking to be reduced. This may be expected due to the strong cross section for electron scattering in many materials, which has produced symmetry breaking in even atomically thin systems (Deb et al., 2020).

The EWIC transform is designed to detect asymmetries, which can arise from specimen tilt besides structural origins. Here, we visualize the effect of tilt using the Ewald sphere, which can be described as an envelope function E(k) multiplied by the reciprocal lattice potential, V(k) (Eq. (2)). A shift of the center of the Ewald sphere introduces a dominant asymmetric term enhancing one part of the diffraction pattern relative to the other. In diffraction space, the Ewald sphere term is multiplied by the potential yielding a convolution of the corresponding real-space terms in both the EWPC and EWIC transforms. The EWPC transform is only weakly sensitive to this off-centering (Padgett et al., 2020) since the smearing of lattice points is symmetrical. This effect is shown schematically in Figure 5a for a model cubic A-B crystal with an off-center polar displacement for the B site.

In the EWIC transform, the tilt manifests as an imaginary dipole term convolved with all the lattice points, as shown for a range of specimen misorientations in Figure 5b. In this figure, the black box indicates the location of the polar dipole and the green circle indicates a characteristic unit-cell distance or lattice site. Effects of crystal tilt in the EWIC transform are easily identifiable because the resulting dipole appears even at the lattice vector (unit-cell) points, such as the ones circled in green, which cannot arise from crystal asymmetry. These dipoles point in the direction of specimen misorientation. Dipoles from the crystal asymmetry, such as those marked with the black rectangle, display some angular deviation with specimen tilt. Because the dipole of the crystal is convolved with the dipole associated with misorientation, the angular deviation is smaller than that for the lattice-vector sites without inherent dipoles. The error in angular deviation and polarization displacement length due to tilt is shown in Figures 5c, 5d. A tilt axis perpendicular to the polarization direction impacts the angular deviation less than a tilt axis parallel to the polarization. With specimen misorientation, tilts less than 5 mrad resulted in less than a 5% error in the dipole length. Correcting for the Ewald sphere off-centering may be possible by multiplying the data by a function that is effectively the inverse of the one describing the Ewald sphere. While we attempted this correction using an Ewald sphere that was extracted using a low-pass filter of the EWPC transform (Padgett et al., 2020), we only saw a reasonably satisfying effect for simulated data—in experimental data, it did not produce reliable results, likely due to noise in both the pattern and extracted Ewald sphere.

A comparison of the robustness of EWIC and IPF with specimen thickness and tilt is shown in Supplementary Figure 1b. As expected, due to the logarithm, the EWIC is significantly more robust to mistilts in both the angular and length deviations measured compared to the IPF. Furthermore, the analytical calculations are compared with Blochwave simulations for specimen mistilt in GaN in Supplementary Figure 2. The results are qualitatively similar for the polar dipoles, although including the effect of specimen thickness in the Blochwaves also introduces larger background signals.

Another source of asymmetry in the diffraction pattern is off-centering of the diffraction pattern on the detector. Such off-centering is inevitable for experimental data, but fortunately, it is easily corrected. This artifact, which is manifested in the appearance of bright spots in one half of the EWIC transform and dark spots in the other half even for subpixel centering inaccuracies, must be corrected during postprocessing by numerically shifting the diffraction pattern to the image center. In practice, finding the diffraction pattern center with subpixel precision can be done in several ways; for example, a relatively simple approach is to minimize the absolute magnitude of the EWIC pattern at lattice sites for different centering corrections (see Methods).

#### Polar Mapping in Ferroelectric Thin Film

Here, we demonstrate the use of the EWPC and EWIC transforms of scanning NBED for mapping the time-averaged local polarization directions in a thin film of tetragonal, ferroelectric PbTiO<sub>3</sub> (Fig. 6). This film is grown on a DyScO<sub>3</sub> substrate that strains the film, generating larger *c*-domains having the polarization vector along the [001] direction normal to the film surface and smaller *a*-domains with polarization pointing in the in-plane [100] direction (Langenberg et al., 2019). Example NBED patterns from each domain type are shown

in Figure 6a. In these patterns, symmetry is broken along [001] and [100] directions for the c- and a-domains, respectively. The cropped EWPC pattern, displaying the interatomic distances, is shown in Figure 6b. Yellow squares mark spots at lattice-vector distances along the c- and a-directions. These spots are sharper than the intraunit-cell spots representing the Pb-Ti distances, which are blurred because of the polar displacements creating shorter and longer distances between Pb and Ti. The EWIC transform, shown in Figure 6c, reveals strong dipole signatures, marked by black squares, at the Pb-Ti distances. Vectors linking the blue and red peaks comprising these dipoles reflect the directions of the relative Ti/ Pb off-center shifts, which define the polarization direction. Furthermore, in the EWIC transform, there is no signal at the lattice sites, indicating that the original NBED pattern exhibits no mistilting or miscentering. Oxygen-cation dipoles can also be observed, although they are less distinct.

EWPC permits localized measurements of the lattice parameters and the cla ratio, as shown in Figure 6d and described previously (Padgett et al., 2020). The orange and purple regions correspond to the c- and a-domains. We measure a cla ratio of  $1.059 \pm 0.001$  (compared to the handbook value of 1.0581) and a flexoelectric rotation of  $86.82^{\circ} \pm 0.02^{\circ}$  between the domains. Theoretically, we expect a rotation of  $86.766^{\circ}$  as calculated from the handbook cla ratio as described in references MacLaren et al., 2005; Farooq et al., 2008. The discrepancies between these numbers likely reflects small miscalibration of the detector and slight differences in the directions of the projector lenses.

The dipole lengths and directions in the EWIC patterns can be used to extract polar displacements, plotted as vectors in Figure 6e. The arrow color reflects the dipole angle, as shown in the histogram of dipole angles in Figure 6e, with the blue and red arrows corresponding to c-domains and a-domains, respectively. The polarization angle exhibits a broad distribution with a standard deviation of about  $\pm 15^{\circ}$ . This spread in polarization is likely due to a combination of flexoelectric rotations, as seen by Catalan et al., 2011, strain relaxation that occurs during TEM lift-out into a thin lamella, and significant spread from the measurement technique. In the middle of the c-domains relatively far from the domain walls, the measured spread in polarization is 10°. The dipole length is  $(19 \pm 4)$  pm, slightly larger than the displacement of 15 pm expected for PbTiO<sub>3</sub>. The reported spread is the standard deviation of the measurements. We attribute this discrepancy to the EWIC overestimating the measured distances when the separation of spots in the dipole is small, leading to overlapping tails (as shown in Fig. 3c). This issue could be caused by undersampling because of a lack of higher-order spots due to the short sampling time and the sample thickness limiting the extent of the Ewald sphere intersection with the diffraction pattern plane. This illustrates how it is critical for the EWIC method to have proper sampling to measure small displacements, and how during data processing we should check the spacings compared to the sampling size and cepstral peak width to ensure the dipole lengths are not overestimated.

#### **Discussion**

In this paper, we describe the use of the imaginary part of the exit wave cepstrum to map polarization in crystals. Because this EWIC approach is based on measuring asymmetries present due to the breakdown of Friedel's law by dynamical

diffraction, it can produce spurious results for specimens with crystal mistilt, high thicknesses, and those with very small polar displacements. This contrasts with the EWPC algorithm, which was remarkably robust to crystal mistilt and thickness.

All diffraction-based methods for measuring polarization fundamentally rely on the breaking of Friedel's law and as such are reliant on the intensity differences of the diffraction pattern (Wicks & Lewis, 1968; Serneels et al., 1973; Tanaka, 1975; Lebeau et al., 2011; Tsuda et al., 2013; Yadav et al., 2019; Deb et al., 2020). Measurement of the intensity differences in diffraction disks can directly provide polarization direction, but additional calculations and simulations are necessary in order to relate that to polarization magnitude (Spence, 1993). The EWIC approach requires no simulations to pull out the magnitude of polar displacements in addition to their directions, making it computationally more convenient. By compiling data from the overall diffraction pattern, not just individual spots, the EWIC technique is also relatively dose efficient. However, to avoid spurious results for very small displacements, either appropriate sampling of EWIC or additional verification from disk intensities and/or simulations is required.

Friedel law breaking can also produce intensity differences in the Kikuchi bands (Marthinsen & Høier, 1988; Bird & Wright, 1989). Recent comparison of Kikuchi band polarization mapping and diffraction intensity mapping suggests that contrast reversal happens for Bragg disks around 0.04° (~0.7 mrad), whereas Kikuchi mapping can tolerate mistilt of up to 0.23° (4 mrad) (Shao et al., 2023). Because EWIC is comparing symmetry breaking in Bragg disk intensities, EWIC is also susceptible to thickness and mistilt artifacts. However, we did not observe a reversal in dipole direction for the EWIC method across the 10 mrad of specimen tilt calculated for the polar spots in Figure 5, or for similar calculations and Blochwave simulations for GaN in Supplementary Figure 2. This apparent suppression of sensitivity to tilt may in part be due to the logarithm, which flattens and separates components such as the Ewald sphere and the lattice. In the EWIC, the Ewald sphere term acts as a convolution on each lattice point, deviating the angle of tilt (not flipping it). The polarization magnitude measured by EWIC deviates less than 5% within 5 mrad of specimen tilt.

Additional scanning diffraction methods to determine polarization include ptychographic reconstruction, which can extract atomic positions, even in the projection direction (Chen et al., 2021). While incredibly powerful, in that it can achieve resolutions limited by thermal vibrations in the crystal, advanced reconstruction techniques are necessary, especially for thicker specimens. Furthermore, it requires significant dose and high sampling (similar to atomic resolution ADF-STEM), compared to NBED-based methods which typically require lower doses and can sample larger regions, at the cost of lower spatial resolution.

#### Conclusion

Here, we outline an algorithm that utilizes the EWIC transform of NBED patterns to map polar displacements at the nanoscale. This technique applies to large classes of technologically relevant materials including ferroelectrics, piezoelectrics, and many two-dimensional materials. The EWIC transform distills the breaking of inversion symmetry in NBED, extracting the directions and magnitudes of the polar

displacements with near-picometer precision. Because EWIC relies on relative diffraction spot intensities, it is sensitive to dynamical diffraction and multiple scattering. Here, it is demonstrated for GaN that we can extract accurate polarity information for thicknesses of up to half of an elastic mean free path. Furthermore, specimen misorientation must be minimized because it introduces additional asymmetry into NBED patterns; fortunately, such artifacts are easy to identify and introduce minimal artifacts below 5 mrad of specimen misorientation. Precession of the electron beam or postprocessing of NBED patterns may mitigate the effects of tilt. The EWIC technique is somewhat less robust to specimen thickness and mistilt compared to the EWPC technique but is still suitable for high-quality STEM samples. We experimentally demonstrate this mapping technique using a PbTiO<sub>3</sub> thin-film specimen with an a/c domain structure to determine the direction and magnitude of the local polarization in a single dataset. The ability of EWIC to provide quantitative and direct measurements of polar displacements over a wide range of length scales makes it useful for characterization of polar materials and devices.

#### **Availability of Data and Materials**

The data that support the findings of this study are available from the corresponding author upon reasonable request.

#### **Supplementary Material**

To view supplementary material for this article, please visit https://doi.org/10.1093/micmic/ozad070.

#### **Acknowledgments**

The authors thank Eric Langenberg, Darrell Schlom, Yu-Tsun Shao, Yimo Han, and Pratiti Deb for specimens and/or useful discussions.

#### Financial Support

Financial support for this work was provided by the U.S. National Institute of Standards and Technology. This work additionally made use of electron microscopy facilities supported by the NSF MRSEC program (DMR-1719875), NSF Cooperative Agreement No. DMR-2039380, and an NSF MRI grant (DMR-1429155).

#### **Conflict of Interest**

The authors declare that they have no competing interest

#### References

Aso R, Kan D, Shimakawa Y & Kurata H (2013). Atomic level observation of octahedral distortions at the perovskite oxide heterointerface. *Sci Rep* 3, 2214. https://doi.org/10.1038/srep02214

Baggari E, Savitzky I, Admasu BH, Kim AS, Cheong J, Hovden S-W, & Kourkoutis R & FL (2018). Nature and evolution of incommensurate charge order in manganites visualized with cryogenic scanning transmission electron microscopy. *Proc Natl Acad Sci USA* 115, 1445–1450. https://doi.org/10.1073/pnas.1714901115

Billinge SJL & Levin I (2007). The problem with determining atomic structure at the nanoscale. *Science* **316**, 561–565. https://doi.org/10.1126/science.1135080

- Bird DM & Wright AG (1989). Phase dependence of Kikuchi patterns. I. Theory. Acta Cryst 45, 104–109 https://doi.org/10. 1107/S0108767388009304
- Borisevich A, Ovchinnikov OS, Chang HJ, Oxley MP, Yu P, Seidel J, Eliseev EA, Morozovska AN, Ramesh R, Pennycook SJ & Kalinin SV (2010). Mapping octahedral tilts and polarization across a domain wall in BiFeO<sub>3</sub> from Z-contrast scanning transmission electron microscopy image atomic column shape analysis. *ACS Nano* 4, 6071–6079. https://doi.org/10.1021/nn1011539
- Bürger J, Riedl T & Lindner JKN (2020). Influence of lens aberrations, specimen thickness and tilt on differential phase contrast STEM images. *Ultramicroscopy* 219, 113118. https://doi.org/10.1016/j.ultramic.2020.113118
- Campanini M, Eimre K, Bon M, Pignedoli CA, Rossell MD & Erni R (2020). Atomic-resolution differential phase contrast STEM on ferroelectric materials: A mean-field approach. *Phys Rev B* 101, 184116. https://doi.org/10.1103/PhysRevB.101.184116
- Catalan G, Lubk A, Vlooswijk AHG, Snoeck E, Magen C, Janssens A, Rispens G, Rijnders G, Blank DHA & Noheda B (2011). Flexoelectric rotation of polarization in ferroelectric thin films. *Nat Mater* 10, 963–967. https://doi.org/10.1038/nmat3141
- Chang HJ, Kalinin SV, Morozovska AN, Huijben M, Chu Y-H, Yu P, Ramesh R, Eliseev EA, Svechnikov GS, Pennycook SJ & Borisevich AY (2011). Atomically resolved mapping of polarization and electric fields across ferroelectric/oxide interfaces by Z-contrast imaging. Advanced Materials 23, 2474–2479. https://doi.org/10. 1002/adma.201004641
- Chen Z, Jiang Y, Shao Y-T, Holtz ME, Odstrčil M, Guizar-Sicairos M, Hanke I, Ganschow S, Schlom DG & Muller DA (2021). Electron ptychography achieves atomic-resolution limits set by lattice vibrations. *Science* 372, 826–831. https://doi.org/10.1126/science. abg2533
- Crewe AV, Wall J & Langmore J (1970). Visibility of single atoms. Science 168, 1338–1340. https://doi.org/10.1126/science.168. 3937.1338
- Deb P, Cao MC, Han Y, Holtz ME, Xie S, Park J, Hovden R & Muller DA (2020). Imaging polarity in two dimensional materials by breaking Friedel's law. *Ultramicroscopy* 215, 113019. https://doi.org/ 11930258X
- Egerton RF (2011). Electron Energy-Loss Spectroscopy in the Electron Microscope, 3rd ed. New York: Plenum Press.
- Eremenko M, Krayzman V, Bosak A, Playford HY, Chapman KW, Woicik JC, Ravel B & Levin I (2019). Local atomic order and hierarchical polar nanoregions in a classical relaxor ferroelectric. *Nat Commun* 10, 2728. https://doi.org/10.1038/s41467-019-10665-4
- Eremenko M, Krayzman V, Gagin A & Levin I (2017). Advancing reverse Monte Carlo structure refinements to the nanoscale. *J Appl Crystallogr* 50, 1561–1570. https://doi.org/1600576717013140
- Farooq MU, Villaurrutia R, MacLaren I, Kungl H, Hoffmann MJ, Fundenberger J-J & Bouzy E (2008). Using EBSD and TEM-Kikuchi patterns to study local crystallography at the domain boundaries of lead zirconate titanate. *J Microsc* 230, 445–454. https://doi.org/10.1111/j.1365-2818.2008.02004.x
- Findlay SD, Shibata N, Sawada H, Okunishi E, Kondo Y, Yamamoto T & Ikuhara Y (2009). Robust atomic resolution imaging of light elements using scanning transmission electron microscopy. Appl Phys Lett 95, 191913. https://doi.org/10.1063/1.3265946
- Han MG, Marshall MSJ, Wu L, Schofield MA, Aoki T, Twesten R, Hoffman J, Walker FJ, Ahn CH & Zhu Y (2014). Interface-induced nonswitchable domains in ferroelectric thin films. Nat Commun 5, 1–9. https://doi.org/10.1038/ncomms5693
- Holtz, M. E. (2022). GitHub EWCC. GitHub. https://github.com/ meganholtz/EWCC.
- Holtz ME, Padgett ES, Steinhardt R, Brooks CM, Meier D, Schlom DG, Muller DA & Mundy JA (2021). Dimensionality-induced change in topological order in multiferroic oxide superlattices. *Phys Rev Lett* 126, 157601. https://doi.org/10.1103/PhysRevLett.126.157601
- Holtz ME, Shapovalov K, Mundy JA, Chang CS, Yan Z, Bourret E, Muller DA, Meier D & Cano A (2017). Topological defects in

- hexagonal manganites: Inner structure and emergent electrostatics. *Nano Lett* 17, 5883–5890. https://doi.org/10.1021/acs.nanolett. 7b01288
- Hovden R, Tsen AW, Liu P, Savitzky BH, El Baggari I, Liu Y, Lu W, Sun Y, Kim P, Pasupathy AN & Kourkoutis LF (2016). Atomic lattice disorder in charge-density-wave phases of exfoliated dichalcogenides (1T-TaS 2). Proc Natl Acad Sci USA 113, 11420–11424. https://doi.org/10.1073/pnas.1606044113
- Howie A (1971). The theory of electron diffraction image contrast. In Electron Microsc. Mater. Science, Valdre U & Zichinchi A (Eds.), pp. 275–300. New York, NY: Academic Press.
- Howie A (1979). Image contrast and localized signal selection techniques. *J Microsc* 117, 11–23. https://doi.org/10.1111/j.1365-2818. 1979.tb00228.x
- Howie A & Whelan MJ (1961). Diffraction contrast of electron microscope images of crystal lattice defects—II. The development of a dynamical theory. Proc R Soc London. Series A. Math Phys Sci 263, 217–237. https://doi.org/10.1098/rspa.1961.0157
- Ishizuka K (1982). Multislice formula for inclined illumination. *Acta Cryst Sect A* 38, 773–779. https://doi.org/10.1107/S0567739482001594.
- Jia C-L, Mi S-B, Urban K, Vrejoiu I, Alexe M & Hesse D (2008). Atomic-scale study of electric dipoles near charged and uncharged domain walls in ferroelectric films. *Nat Mater* 7, 57–61. https://doi.org/10.1038/nmat2080
- Jia C-L, Nagarajan V, He J-Q, Houben L, Zhao T, Ramesh R, Urban K & Waser R (2007). Unit-cell scale mapping of ferroelectricity and tetragonality in epitaxial ultrathin ferroelectric films. Nat Mater 6, 64–69. https://doi.org/10.1038/nmat1808
- Kimoto K, Asaka T, Yu X, Nagai T, Matsui Y & Ishizuka K (2010). Local crystal structure analysis with several picometer precision using scanning transmission electron microscopy. *Ultramicroscopy* 110, 778–782. https://doi.org/10.1016/j.ultramic.2009.11.014
- Kirkland EJ (2020). Advanced Computing in Electron Microscopy. Cham: Springer International Publishing.
- Kirkland EJ, Loane RF & Silcox J (1987). Simulation of annular dark field stem images using a modified multislice method. *Ultramicroscopy* **23**, 77–96. https://doi.org/10.1016/0304-3991(87)90229-4
- Kumar A, Baker JN, Bowes PC, Cabral MJ, Zhang S, Dickey EC, Irving DL & LeBeau JM (2021). Atomic-resolution electron microscopy of nanoscale local structure in lead-based relaxor ferroelectrics. *Nat Mater* 20, 62–67. https://doi.org/10.1038/s41563-020-0794-5
- Langenberg E, Saha D, Holtz ME, Wang J-J, Bugallo D, Ferreiro-Vila E, Paik H, Hanke I, Ganschow S, Muller DA, Chen L-Q, Catalan G, Domingo N, Malen J, Schlom DG & Rivadulla F (2019). Ferroelectric domain walls in PbTiO<sub>3</sub> are effective regulators of heat flow at room temperature. *Nano Lett* 19, 7901–7907. https://doi.org/10.1021/acs.nanolett.9b02991
- Lazić I, Bosch EGT & Lazar S (2016). Phase contrast STEM for thin samples: Integrated differential phase contrast. *Ultramicroscopy* 160, 265–280. https://doi.org/10.1016/j.ultramic.2015.10.011
- LeBeau JM, D'Alfonso AJ, Findlay SD, Stemmer S & Allen LJ (2009).
  Quantitative comparisons of contrast in experimental and simulated bright-field scanning transmission electron microscopy images. *Phys Rev B* 80, 174106. https://doi.org/10.1103/PhysRevB.80.174106
- Lebeau JM, D'Alfonso AJ, Wright NJ, Allen LJ & Stemmer S (2011). Determining ferroelectric polarity at the nanoscale. *Appl Phys Lett* **98**, 98–101. https://doi.org/10.1063/1.3549300
- Liu Z, Yang B, Cao W, Fohtung E & Lookman T (2017). Enhanced energy storage with polar vortices in ferroelectric nanocomposites. *Phys Rev Appl* 8, 034014. https://doi.org/10.1103/PhysRev Applied.8.034014
- MacLaren I, Schmitt LA, Fuess H, Kungl H & Hoffmann MJ (2005). Experimental measurement of stress at a four-domain junction in lead zirconate titanate. *J Appl Phys* 97, 094102. https://doi.org/10.1063/1.1886910
- MacLaren I, Wang L, McGrouther D, Craven AJ, McVitie S, Schierholz R, Kovács A, Barthel J & Dunin-Borkowski RE (2015). On the

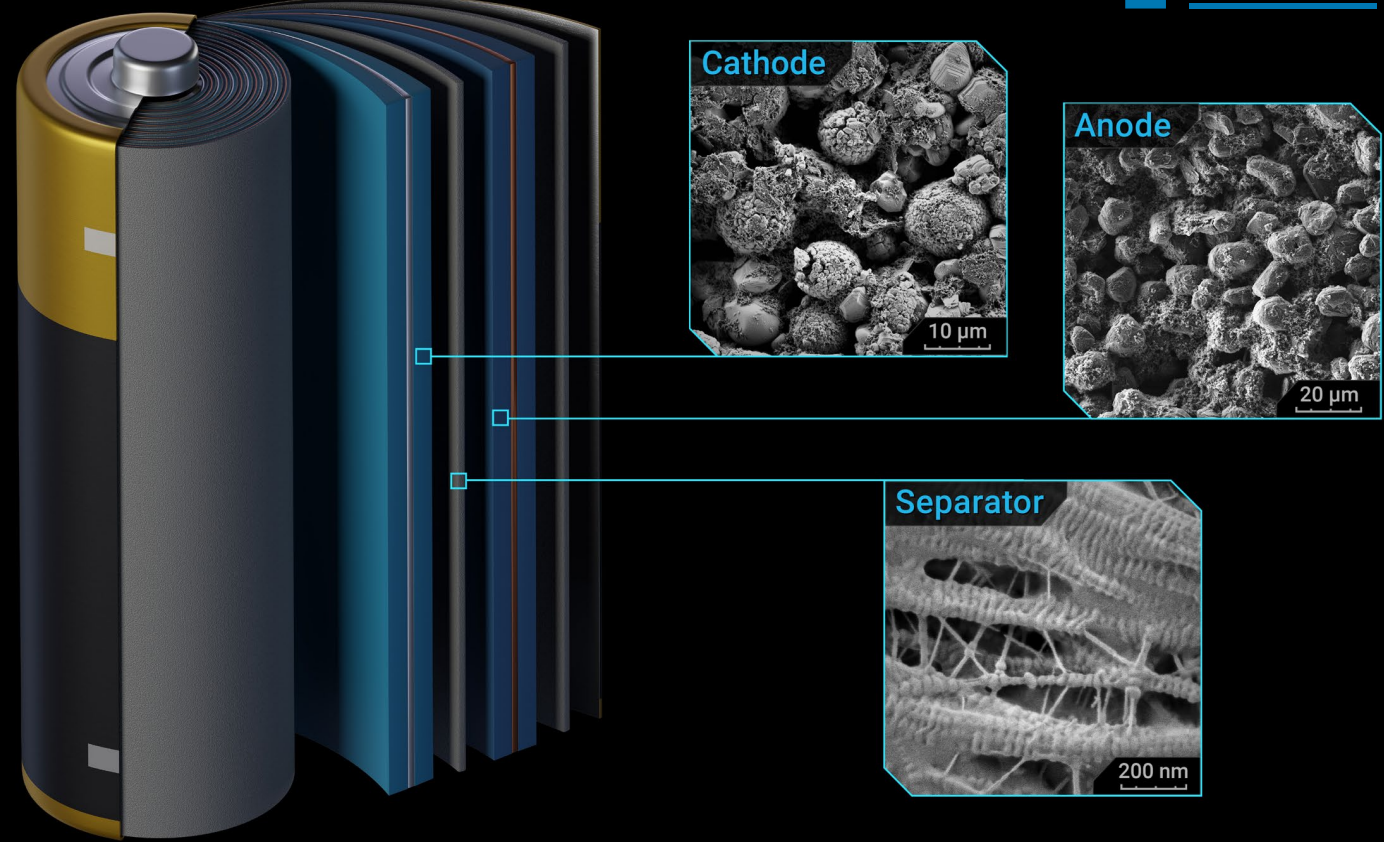
origin of differential phase contrast at a locally charged and globally charge-compensated domain boundary in a polar-ordered material. *Ultramicroscopy* **154**, *57–63*. https://doi.org/10.1016/j.ultramic. 2015.03.016

- MacLaren I, Wang L, Morris O, Craven AJ, Stamps RL, Schaffer B, Ramasse QM, Miao S, Kalantari K, Sterianou I & Reaney IM (2013). Local stabilisation of polar order at charged antiphase boundaries in antiferroelectric (Bi 0.85 Nd 0.15)(Ti 0.1 Fe 0.9)O 3. APL Mater 1, 021102. https://doi.org/10.1063/1.4818002
- Malis T, Cheng SC & Egerton RF (1988). EELS log-ratio technique for specimen-thickness measurement in the TEM. *J Electron Microsc Tech* 8, 193–200. https://doi.org/10.1002/jemt.1060080206
- Marthinsen K & Høier R (1988). On the breakdown of Friedel's law in electron backscattering channelling patterns. *Acta Crystallogr A Found Crystallogr* 44, 700–707. https://doi.org/10.1107/S0108767388004532.
- Miyake S & Uyeda R (1955). Friedel's law in the dynamical theory of diffraction. Acta Crystallogr 8, 335–342. https://doi.org/10.1107/ S0365110X55001023
- Muller DA, Kirkland EJ, Thomas MG, Grazul JL, Fitting L & Weyland M (2006). Room design for high-performance electron microscopy. *Ultramicroscopy* **106**, 1033–1040. https://doi.org/10.1016/j.ultramic.2006.04.017
- Nahas Y, Prokhorenko S, Louis L, Gui Z, Kornev I & Bellaiche L (2015). Discovery of stable skyrmionic state in ferroelectric nanocomposites. Nat Commun 6, 1–6. https://doi.org/10.1038/ ncomms9542
- Naumov II, Bellaiche L & Fu H (2004). Unusual phase transitions in ferroelectric nanodisks and nanorods. *Nature* **432**, 737–740. https://doi.org/10.1038/nature03107
- Nelson CT, Winchester B, Zhang Y, Kim S-J, Melville A, Adamo C, Folkman CM, Baek S-H, Eom C-B, Schlom DG, Chen L-Q & Pan X (2011). Spontaneous vortex nanodomain arrays at ferroelectric heterointerfaces. *Nano Lett* 11, 828–834. https://doi.org/10.1021/nl1041808
- Ophus C (2019). Four-dimensional scanning transmission electron microscopy (4D-STEM): From scanning nanodiffraction to ptychography and beyond. *Microsc Microanal* 25, 563–582. https://doi.org/10.1017/S1431927619000497
- Padgett E, Holtz ME, Cueva P, Shao Y-T, Langenberg E, Schlom DG & Muller DA (2020). The exit-wave power-cepstrum transform for scanning nanobeam electron diffraction: Robust strain mapping at subnanometer resolution and subpicometer precision. Ultramicroscopy 214, 112994. https://doi.org/10.1016/j.ultramic.2020.112994
- Patterson AL (1934). A Fourier series method for the determination of the components of interatomic distances in crystals. *Phys Rev* 46, 372–376. https://doi.org/10.1103/PhysRev.46.372
- Reimer L & Kohl H. (2008). Transmission electron microscopy physics of image formation. Springer.
- Schilling A, Byrne D, Catalan G, Webber KG, Genenko YA, Wu GS, Scott JF & Gregg JM (2009). Domains in ferroelectric nanodots. Nano Lett 9, 3359–3364. https://doi.org/10.1021/nl901661a
- Schulz H & Thiemann KH (1977). Crystal structure refinement of AlN and GaN. Solid State Commun 23, 815–819. https://doi.org/10.1016/0038-1098(77)90959-0
- Serneels R, Snykers M, Delavignette P, Gevers R & Amelinckx S (1973).
  Friedel's law in electron diffraction as applied to the study of domain structures in non-centrosymmetrical crystals. *Phys Status Solidi (b)* 58, 277–292. https://doi.org/10.1002/pssb.2220580127
- Shao Y-T, Das S, Hong Z, Xu R, Chandrika S, Gómez-Ortiz F, García-Fernández P, Chen L-Q, Hwang HY, Junquera J, Martin LW, Ramesh R & Muller DA (2023). Emergent chirality in a polar meron to skyrmion phase transition. *Nat Commun* 14, 1355. https://doi.org/10.1038/s41467-023-36950-x

Spence JCH (1993). On the accurate measurement of structure-factor amplitudes and phases by electron diffraction. *Acta Crystallogr* **49**, 231–260. https://doi.org/10.1107/S0108767392005087

- Spence JCH (2013). *High-Resolution Electron Microscopy*. Oxford University Press.
- Stemmer S, Streiffer SK, Ernst F & Rühle M (1995a). Atomistic structure of 90° domain walls in ferroelectric PbTiO 3 thin films. *Philosophical Magazine A* 71, 713–724. https://doi.org/10.1080/01418619508244477
- Stemmer S, Streiffer SK, Ernst F, Rühle M, Hsu W-Y & Raj R (1995b). Domain configurations in ferroelectric PbTiO3 thin films: The influence of substrate and film thickness. *Solid State Ionics* 75, 43–48. https://doi.org/10.1016/0167-2738(94)00151-H
- Tanaka M (1975). Contrast of 180° domains of PbTiO3 in an electron microscopic image. *Acta Crystallographica Section A: Crystal Physics, Diffraction, Theor General Crystallogr* **31**, 59–63.
- Tate MW, Purohit P, Chamberlain D, Nguyen KX, Hovden R, Chang CS, Deb P, Turgut E, Heron JT, Schlom DG, Ralph DC, Fuchs GD, Shanks KS, Philipp HT, Muller DA & Gruner SM (2016). High dynamic range pixel array detector for scanning transmission electron microscopy. *Microsc Microanal* 22, 237–249. https://doi.org/10.1017/S1431927615015664
- Tsuda K & Tanaka M (1999). Refinement of crystal structural parameters using two-dimensional energy-filtered CBED patterns. *Acta Crystallogr* 55, 939–954. https://doi.org/10.1107/S0108767399005401
- Tsuda K, Yasuhara A & Tanaka M (2013). Two-dimensional mapping of polarizations of rhombohedral nanostructures in the tetragonal phase of BaTiO 3 by the combined use of the scanning transmission electron microscopy and convergent-beam electron diffraction methods. *Appl Phys Lett* **103**, 082908. https://doi.org/10.1063/1.4819221
- Voyles PM, Muller DA, Grazul JL, Citrin PH & Gossmann H-JL (2002). Atomic-scale imaging of individual dopant atoms and clusters in highly n-type bulk Si. *Nature* 416, 826–829. https://doi.org/ 10.1038/416826a
- Wicks BJ & Lewis MH (1968). Direct observations of ferroelectric domains in lithium niobate. *Phys Status Solidi (b)* **26**, 571–576. https://doi.org/10.1002/pssb.19680260221
- Xu R, Huang J, Barnard ES, Hong SS, Singh P, Wong EK, Jansen T, Harbola V, Xiao J, Wang BY, Crossley S, Lu D, Liu S & Hwang HY (2020). Strain-induced room-temperature ferroelectricity in SrTiO3 membranes. *Nat Commun* 11, 3141. https://doi.org/10. 1038/s41467-020-16912-3
- Yadav AK, Nelson CT, Hsu SL, Hong Z, Clarkson JD, Schlepütz CM, Damodaran AR, Shafer P, Arenholz E, Dedon LR, Chen D, Vishwanath A, Minor AM, Chen LQ, Scott JF, Martin LW & Ramesh R (2016). Observation of polar vortices in oxide superlattices. *Nature* 530, 198–201. https://doi.org/10.1038/nature16463
- Yadav AK, Nguyen KX, Hong Z, García-Fernández P, Aguado-Puente P, Nelson CT, Das S, Prasad B, Kwon D, Cheema S, Khan AI, Hu C, Íñiguez J, Junquera J, Chen LQ, Muller DA, Ramesh R & Salahuddin S (2019). Spatially resolved steady-state negative capacitance. *Nature* 565, 468–471. https://doi.org/10.1038/s41586-018-0855-y
- Zheng Y, Wang B & Woo CH (2007). Effects of interface dislocations on properties of ferroelectric thin films. *J Mech Phys Solids* 55, 1661–1676. https://doi.org/10.1016/j.jmps.2007.01.011
- Zhou D, Müller-Caspary K, Sigle W, Krause FF, Rosenauer A & van Aken PA (2016). Sample tilt effects on atom column position determination in ABF-STEM imaging. *Ultramicroscopy* 160, 110–117. https://doi.org/10.1016/j.ultramic.2015.10.008
- Zuo JM & Spence JCH (2017). Advanced Transmission Electron Microscopy. New York, NY: Springer New York.





# **TESCAN Solutions** for Battery Industry

Power your Advanced Battery Technology and Research with TESCAN Solutions



info.tescan.com/batteries

Scan for more information